ARMA 17- 496

Real-time monitoring of heterogeneous fractures in rock: an experimental study

Pourahmadian, F.

Department of Civil, Environmental, and Architectural Engineering, University of Colorado Boulder, CO, USA

Guzina, B.B.

Department of Civil, Environmental, and Geo- Engineering, University of Minnesota, Minneapolis, MN, USA

ABSTRACT: This study investigates the elastic anatomy of fractures in rock using full wavefield measurements. In this spirit, a 3-step experimental campaign is pursued in a laboratory setting, namely: (1) full-field ultrasonic testing of the intact rock, (2) fracturing, and (3) ultrasonic interrogation of the fractured rock. Experiments are performed on a slab-like prismatic specimen of charcoal granite. The sample is illuminated under the plane stress condition, prior and posterior to fracturing, by a shear piezoelectric transducer at 10 and 30kHz. The (in-plane) velocity response of the rock is monitored via the 3D Scanning Laser Doppler Vibrometer over a rectangular region in the fracture neighborhood. Upon proper signal processing, (i) the maps of elastic modulus in the specimen (before and after fracturing) is computed via elastography, exposing the geometric and elastic properties of the process zone; (ii) the fracture geometry is reconstructed, and (iii) profiles of shear and normal specific stiffness at the fracture interface are identified.

1. INTRODUCTION

Fracturing-induced damage in rock and its elastic attributes, namely: (i) the modified material properties in the damage zone and (ii) the heterogeneous contact condition at the fracture interface, are the subject of mounting interest in various aspects of geophysical science and technology including energy production from unconventional resources (gas/geothermal) (Baird et al. 2013, Verdon and Wustefeld 2013, Taron and Elsworth 2010), environmental protection (Place et al. 2014), seismology (McLaskey et al. 2012), and mining (Gu et al. 1993). The variation of elastic moduli in the damage zone may trigger aseismic slip along rock faults (Calo' et al., 2011). Furthermore, such non-uniform stress distribution gives rise to a heterogeneous elastic contact at the boundary of fractures and faults, that is often parametrized in terms of a distributed (shear and normal) specific stiffness, relating the contact traction to the jump in displacements across the interface (Schoenberg, 1980). The interfacial stiffness – strongly correlated with the surface roughness, static pre-stress and material properties of the bulk rock (and pore/interfacial fluid) (Pyrak-Nolte and Morris 2000) – plays a critical role in the stability and strength of rock discontinuities, and controls the key characteristics of fracture networks in reservoirs. In particular, the inhomogeneous contact condition is responsible for the progressive failure along discontinuities that may occur well before the frictional resistance of the entire interface is surpassed (Hedayat et. al., 2014; Eberhardt et al., 2004). Moreover, the hydraulic properties e.g. fluid conductivity of subsurface discontinuities is directly connected to the elastic nature of their interface (Pyrak-Nolte and Nolte 2016). Therefore, a proper *elastic* representation of fractures in the continuum models of the subsurface may lead to better understanding of subterranean fluid flow e.g. through the fractured reservoirs, and thus, enhance the (gas/geothermal) reservoir prognosis (Pyrak-Nolte and Nolte 2016). On the other hand, the marriage between such "enriched" models of discontinuity and active seismic imaging tools (Pourahmadian et. al., 2015, 2016) opens a path forward for finding timely precursors of instability along rock faults. This work aims to decipher the elastic nature of fracturing in rock in a laboratory setting. In this spirit, a 3-step experimental campaign is designed by taking advantage of the 3D Scanning Laser Doppler Vibrometer (SLDV) that is capable of monitoring triaxial particle velocity, with frequencies up to 1MHz, over the surface of rock specimens with 0.1mm spatial resolution and O(nm) displacement accuracy. Full-field ultrasonic measurements are performed prior and posterior to fracturing the specimen which are then used to quantify (a) the variation of the sample's elastic constants due to fracturing, and (b) the induced fracture geometry and its heterogeneous interfacial condition.

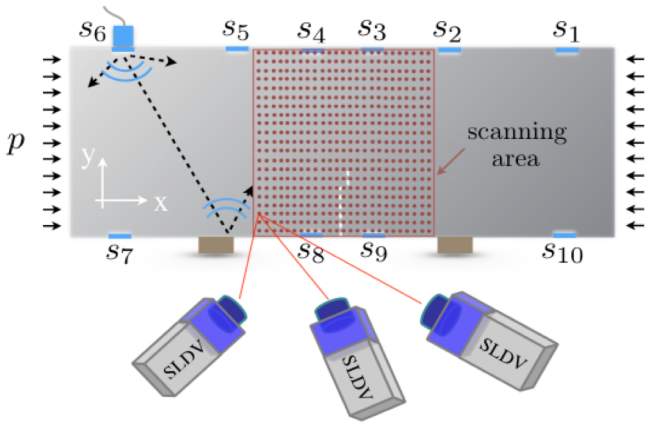

Figure 1. Schematic of the ultrasonic sensing configuration for full-field characterization of the intact and fractured rock: the specimen is under normal compression p, while shear waves are sequentially induced in the sample at source locations $\{s_1, s_2, \dots, s_{10}\}$. and measured by the 3D SLDV.

2. EXPERIMENTAL SETUP

Experiments are performed in three steps on a slab-like prismatic specimen of charcoal granite with dimensions 0.96m × 0.3m × 0.03m whose material properties are characterized by the mass density ρ=2750kg/m^3, nominal Poisson's ratio ν=0.23, and Young's modulus E = 62.56GPa. **Step 1** of the experimental program is performed prior to fracturing the rock where the *intact* granite slab is held by the supports shown in Fig. 2 and the compression frame is detached. The ultrasonic tests are then followed according to Figs. 1 and 3 where $p = 0$ and the sample is illuminated by in-plane shear waves via a piezoelectric transducer attached to the granite at one of the designated source locations $\{s_1, s_2, \dots, s_{10}\}$. The excitation wavelet is a modulated five-cycle burst with central frequency $f_c = 10, 30$kHz at every source location. In this vein, Fig. 4 compares the affiliated "reference" waveforms (produced in the signal generator) and the resulting particle velocities v_x (in x- direction) induced in the immediate vicinity of the transducer measured by the 3D SLDV.

Note that the length of specimen is almost one meter catering for the propagation of low-frequency waves e.g. f_c = 10kHz through the sample. Moreover, the slab thickness of 0.03m is at least three times smaller than the probing wavelength, which allows for the plane-stress approximation at the designated excitation. In this setting, the compressional (P-) and shear (S-) wave velocities in the granite slab are, respectively, $c_p = \sqrt{E/(\rho(1\text{-}\nu^2))}$ = 4901 m/s, and $c_s = \sqrt{E/(2\rho(1+\nu))}$ = 3041m/s. With reference to Fig. 3, the produced wave motion in the granite slab is then measured via the 3D SLDV over a 32.8cm × 29.3cm scanning area shown in Fig. 1 where the scanning resolution is about four scan-points per 2.54cm. Note that the SLDV-captured surface motion is

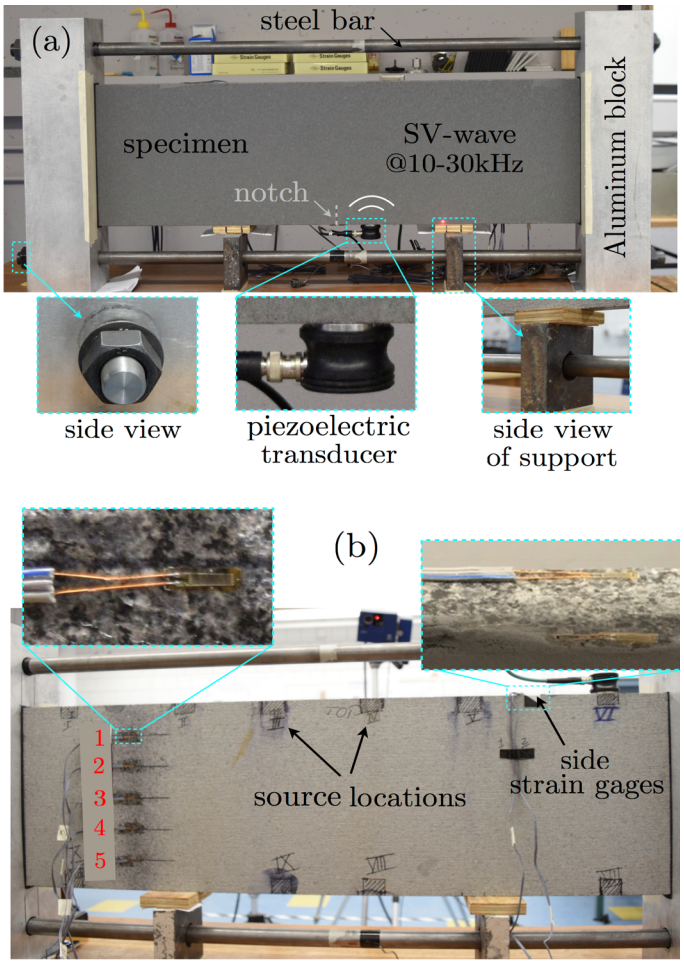

Figure 2. Prestressed rock specimen: fractured granite slab held in the compression fixture, and (b) specimen's backside where attached strain gages quantify/control the applied static prestress.

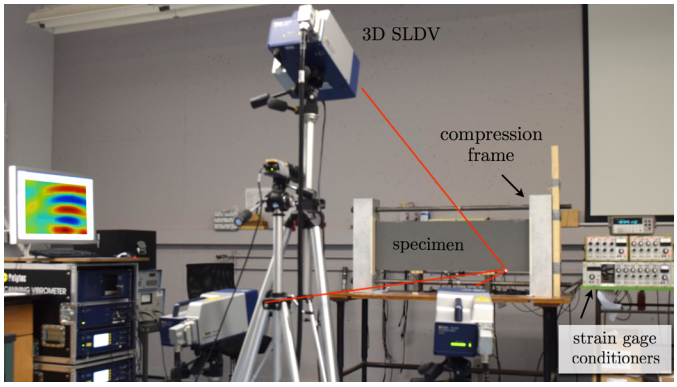

Figure 3. Ultrasonic testing of a fractured rock: the specimen is prestressed up to 1.5MPa (in the compression frame) when in-plane shear waves are generated by a piezoelectric transducer at 10-30kHz; thus-induced wave motion is measured by the 3D SLDV in terms of the particle velocities (in the x- and y-directions) on the sample surface.

considered uniform through the thickness of the granite slab, thanks to the plane-stress approximation. In addition, thus-obtained ultrasonic measurements represent the "baseline" wave motion in the intact

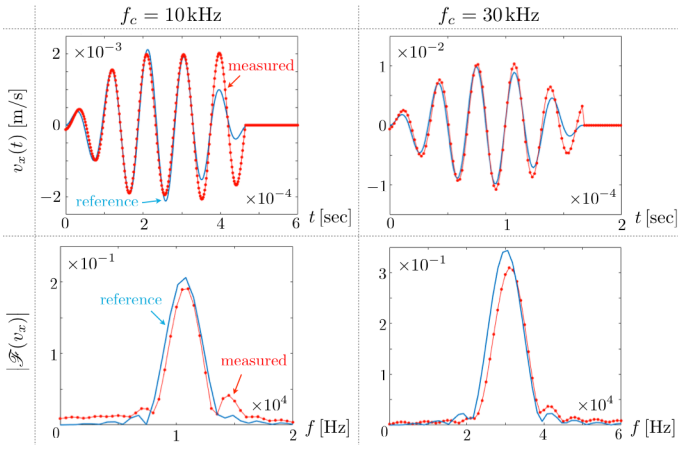

Figure 4. Reference (solid) *vs*. SLDV-measured (dotted) excitation: time history and frequency spectrum of the *input* (velocity) wavelets at the center frequencies $f_c = 10, 30\text{kHz}$.

granite, see right panels in Fig. 5, that will be used (i) to recover the intrinsic "heterogeneity" of the rock elastic parameters prior to fracturing, and (ii) to directly compute (from the SLDV data later in **Step 3**) the scattered field due to the *fracturing-induced* damage in the specimen.

In preparation for **Step 2** of the experimental program, a notch of length 4cm is manufactured at the lower mid-length of the specimen, see Fig. 2 (a). The sample is fractured in the three-point-bending (3PB) configuration in a 1000kN MTS load frame, continued approximately up to 65% of the maximum load in the post-peak regime. The specimen is then transferred to the compression frame (Fig. 2 (a)) for complementary ultrasonic testing.

Aiming at the full-field characterization of the fractured rock, experiments in **Step 3** are performed in a sensing configuration shown in Fig. 1 that is essentially the same testing setup as in **Step 1** in terms of the transducer locations, illuminating wavelet and scanning area. In this step, however, the normal compression may assume a non-zero value of $p = 1.5\text{MPa}$ (in addition to $p = 0$) in order to study the impact of static prestress on (a) the contact law at the fracture interface, and (b) the spatial distribution of elastic properties of the *fractured* rock. As illustrated in Fig. 2 (a), the normal stress p is applied to the specimen via the compression fixture. Thus-induced normal pressure and its distribution along the width of the specimen is then quantified by using the Young's modulus of the rock and five strain-gage readings on the sample's back. Furthermore, the variations of p through the slab's thickness – e.g. due to out of plane moments triggered by the misalignments of the compression frame, is monitored via two longitudinal strain gages placed on the specimen edge across each side. It is observed that such variations (along the thickness) are less than 10% of the average value of p. With reference to Fig. 5, the SLDV measurements in **Step 3** (right panel) are known as the "total" fields whose comparison with their associated free fields (left panel), obtained in **Step 1**, reveals the

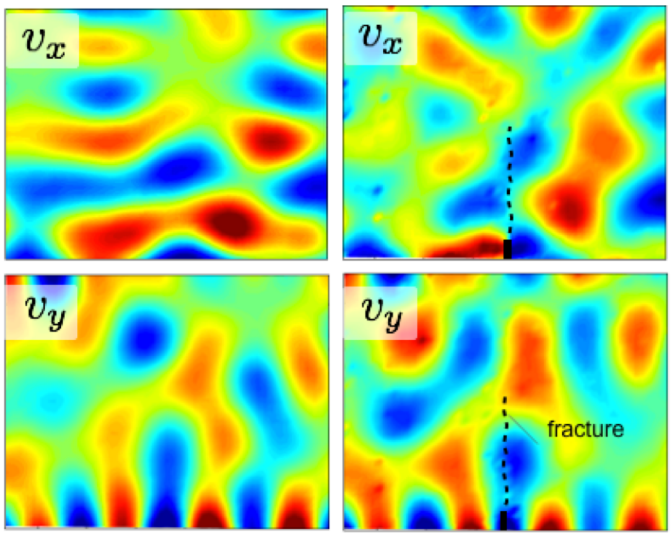

Figure 5. A time snapshot of the particle velocity fields, in x- and y- directions, measured by the 3D SLDV (in a 32.8cm × 29.3cm scanning window) before (left panel) and after (right panel) fracturing the granite specimen. the input (velocity) wavelet is centered at frequency $f_c = 30\text{kHz}$.

scattering characteristics of the induced damage. In particular, one may note that the surface-breaking notch is a major scatterer of the Rayleigh waves, while the fracture's connected segments give rise to a much weaker scattering due to the interfacial interactions to be quantified in the sequel.

3. RESULTS AND DISCUSSION

To characterize the fracturing-induced damage in rock, the ultrasonic measurements acquired in **Step 1** and **Step 3** are processed - according to the algorithm proposed in (Pourahmadian and Guzina, 2016), namely: (i) to recover the spatial distribution of Young's modulus in the granite specimen prior and posterior to fracturing the sample, by invoking the medical imaging technique known as elastography (Ophir, 1999; Barbone 2004); This exposes perturbations in the rock's elastic properties e.g. due to micro-cracking in the damage zone; (ii) to reconstruct the support of the induced fracture, and (iii) to non-parametrically uncover the contact behavior at the fracture interface, leading to its proper linearization and thus identification of the affiliated interfacial stiffness profiles (in shear and normal directions). In this spirit, the following results are obtained. To recover the fracture geometry, the gradient of the measured particle-velocity fields (v_x, v_y) , Fig. 5 (right), is numerically computed at every snapshot in time, whose infinity-norm is then integrated over the entire time span. Thus-computed fields associated with every source location $\{s_1, s_2, \dots, s_{10}\}$ (Fig. 1) and excitation frequency (10 and 30kHz) are then superimposed, and the resulting plots are shown in Fig. 6 where the loci of scan points with the highest (cumulative) jump values i.e. gradient canvases the support of the hidden fracture.

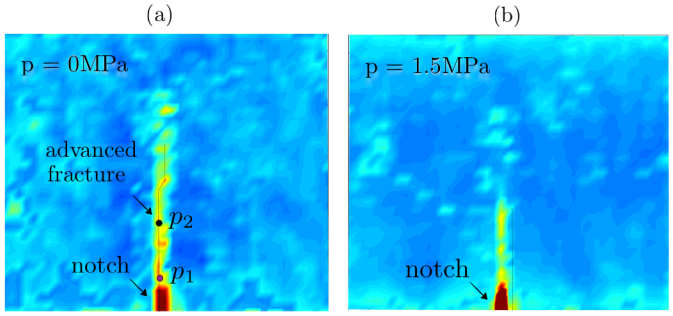

Figure 6. Reconstructed fracture geometry from the SLDV-captured particle velocities in a 32.8cm × 29.3cm scanning window (in **Step 3**): (a) where the normal compression is zero $p = 0$ (see Fig. 1), and (b) when the specimen is under a normal prestress of $p = 1.5$MPa, "closing" the near-tip segment of the existing interface, recovered in (a), which makes it invisible to the ultrasonic waves.

Following the elastography approach, the evolution of rock's elastic modulus due to fracturing is computed according to (Pourahmadian and Guzina, 2016) and the spatial distribution of E in (a) the intact specimen, and (b) fractured sample are illustrated in Fig. 7. Based on these results, the damage zone - identified with the area in the fracture neighborhood where the elastic modulus significantly decreases e.g. due to micro-cracking is characterized by the width of 25mm in the fractured specimen subject to 0MPa normal prestress. This complies with the previously reported width of 10-20mm for the process zone in charcoal granite using acoustic emission approach (Zietlow, 1998).

These findings cater for a robust estimation of stresses in rock which, given the fracture geometry (Fig. 6), enables the computation of shear and normal tractions (t_s, t_n) along the fracture edge. One may also compute the profile of displacement discontinuity across the fracture $(\llbracket u_s \rrbracket, \llbracket u_n \rrbracket)$ known as the fracture opening displacement (FOD), from the smoothed wavefields computed from the SLDV measurements. Now that the pertinent state variables are identified, one may *non-parametrically* retrieve the "true" contact law at the fracture interface through studying the traction versus FOD plots in both shear and normal directions. It should be mentioned that in these experiments (a) the intended nanometer-scale shear (resp. normal) FOD does not allow for the intrinsic nonlinear mechanisms, attributed to friction (resp. impact) (Pourahmadian et. al., 2012), to fully develop at the interface (as on the microscale), which caters for the ensuing linearization of the contact condition. In this vein, the contact law is interpreted in terms of the "linear-slip" model (Schoenberg, 1980) endowed with the spatially varying shear and normal stiffness profiles $(k_s\ k_n)$. For the purpose of model identification, the normal and shear tractions along with their respective FOD are transformed to the frequency domain i.e. by way of Fourier transform $\mathcal{F}(.)$.

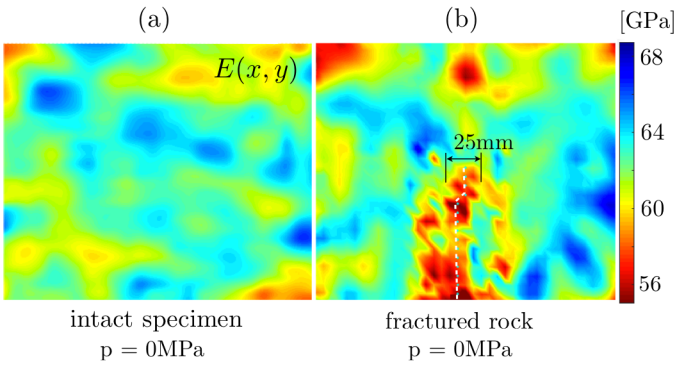

Figure 7. Reconstructed distribution of elastic modulus in a 32.8cm × 29.3cm scanning window using SLDV data of $f_c =$ 30kHz: (a) prior to fracturing the sample (**Step 1**), (b) after fracturing the specimen where the normal prestress $p = 0$MPa (**Step 3**).

Fig. 8 investigating the accuracy of the linear slip model as a true representative of the contact behavior. In this regard, while the equilibrium of the linearized contact condition appears to be reasonable, this model is obviously deficient in capturing the true dynamics of the interface even at such small scales. The identification procedure is repeated for the SLDV-data captured at every source location $\{s_1, s_2, \dots, s_{10}\}$ (in **Step 3**). The mean and standard deviation of the resulting distributions are then calculated and shown in Figs. 9 and 10 for the normal prestress of $p = 0$,1.5MPa, and the excitation frequency of 10, 30kHz. To expose the damage-induced perturbations in the contact behavior, the tractions are calculated using both the nominal elastic modulus, i.e. E=62.56GPa, and the "true" distributions of E in the damage zone shown in Fig. 7 (b).

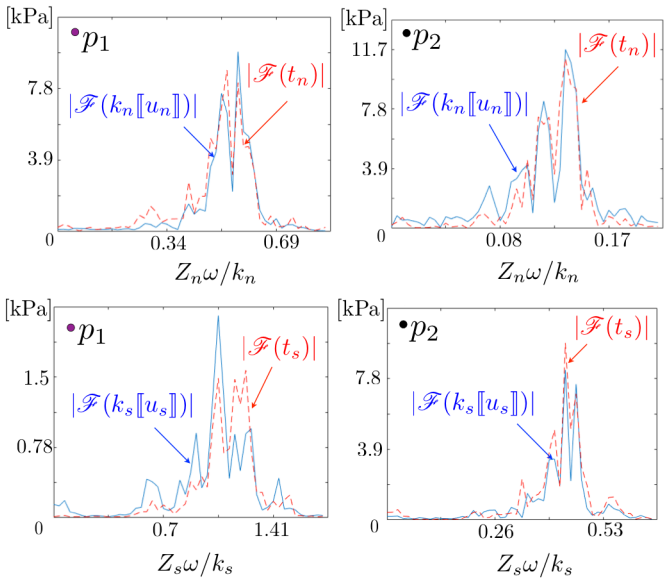

Figure 8. Balance of the "linear slip" contact condition (Schoenberg, 1980) in the frequency domain, i.e. $\mathcal{F}(t_\alpha) = \mathcal{F}(k_\alpha[\![u_\alpha]\!])$, with k_α $(\alpha = s, n)$ denoting the interfacial stiffness in shear and normal directions, at two points p_1 and p_2, shown in Fig. 6 (a), along the fracture edge. The frequency spectrum is pertinent to the source wavelet of $f_c =$ 30kHz and the normal prestress is zero i.e. $p = 0$Mpa.

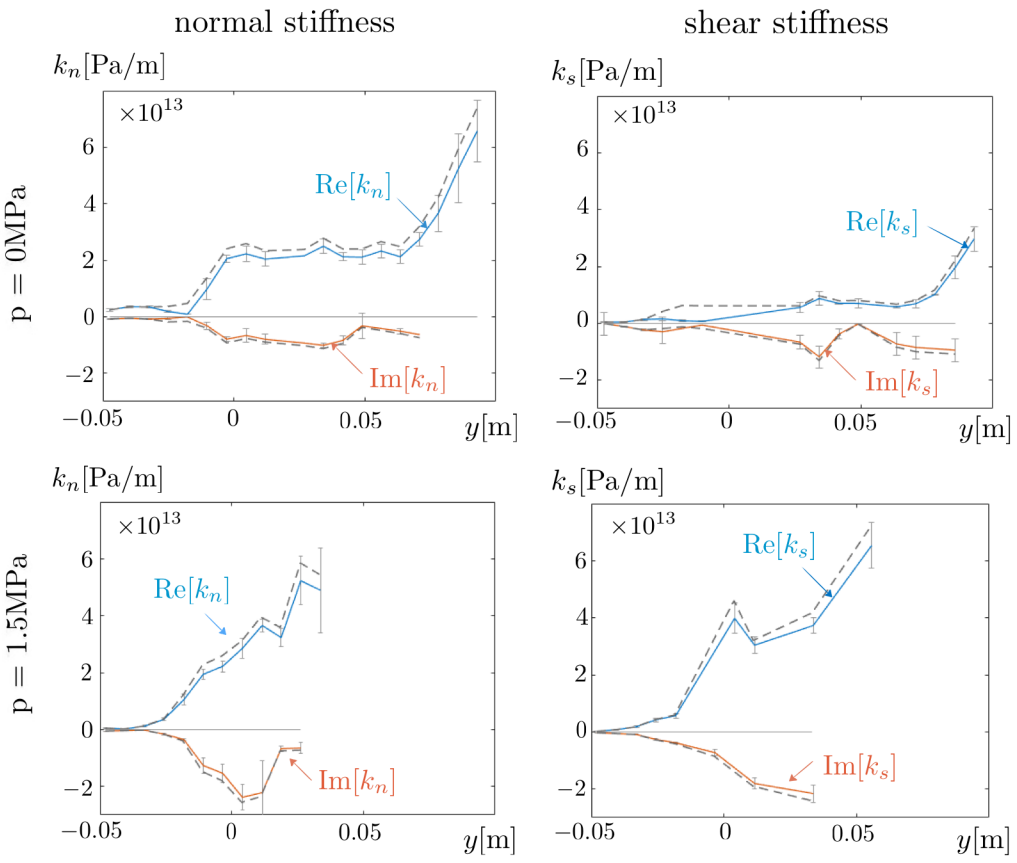

Figure 9. Heterogeneous distribution of normal (left) and shear (right) specific stiffness along the fracture edge - furnished by the frequency spectrums of FOD and traction where the latter is identified by adopting the *nominal* Young's modulus: real and imaginary mean profiles (solid lines) and their affiliated standard deviations (error bars) computed from ten reconstructed distributions associated with the source locations$\{s_1, s_2, \dots, s_{10}\}$. The excitation wavelet is centered at 30kHz, and the fracture is under either 0MPa (top) or 1.5MPa (bottom) of normal prestress.

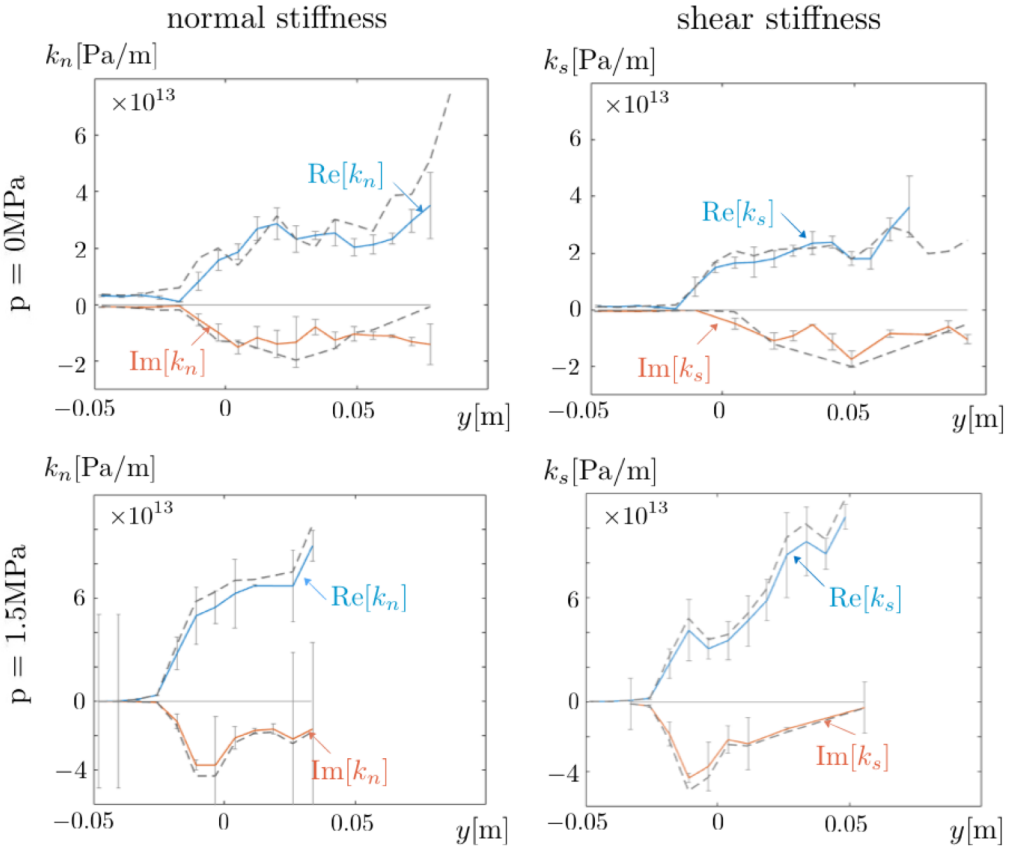

Figure 10. Heterogeneous distribution of normal (left) and shear (right) specific stiffness along the fracture edge - furnished by the frequency spectrums of FOD and traction where the latter is identified by adopting the *nominal* Young's modulus: real and imaginary mean profiles (solid lines) and their affiliated standard deviations (error bars) computed from ten reconstructed distributions associated with the source locations$\{s_1, s_2, \dots, s_{10}\}$. The excitation wavelet is centered at 10kHz, and the fracture is under either 0MPa (top) or 1.5MPa (bottom) of normal prestress.

Pertaining to Figs. 9 and 10, one may note that (i) the near-zero segments of the identified profiles correspond to the notch, (ii) the real parts of both shear and normal specific stiffness increase as the fracture enters the process zone and closes, (iii) the uncertainty of the recovered values i.e. their associated standard deviation increases toward the fracture tip as the FOD is vanishing, (iii) the imaginary part of specific stiffness is a representative of energy dissipation at the interface which, in such small-scale regimes of motion, is expected to be minute and remarkably contaminated by uncertainty; Nonetheless, the recovered imaginary profiles tend to systematically decrease around the tip owing to the infinitesimal relative motion between the two faces of fracture, (iv) at p= 1.5MPa, the ultrasonic waves can only detect a segment of the actual fracture, as shown in Fig. 6 (b), due to compression; This manifests itself, here, as a sharp growth of the specific stiffness both in shear and normal directions that is due to a significant increase in the actual contact area at the interface, brought about by the applied static compression.

4. SUMMARY

In this paper, full-field sensory data are used to (i) compute the maps of elastic modulus in the rock specimen (before and after fracturing) via a technique known as elastography; (ii) identify the fracture geometry as the support of persistent spatial discontinuities in the transient SLDV fields; (iii) expose the fracture's primal (traction-displacement jump) contact behavior, and (iv) identify via Fourier analysis its effective profiles of complex-valued, shear and normal specific stiffness. The results are verified for self-consistency at several key stages of the analysis, and are found to conform with expected trends in terms of the interfacial fracture response to seismic waves.

REFERENCES

1. Baird, A.F., J.M. Kendall, J.P. Verdon, A.Wuestefeld, T.E. Noble, Y. Li, M. Dutko, and Q.J. Fisher. 2013. Monitoring increases in fracture connectivity during hydraulic stimulations from temporal variations in shear wave splitting polarization. *Geophys. J. Int.*
2. Barbone, P.E., N.H. Gokhale. 2004. Elastic modulus imaging: on the uniqueness and nonuniqueness of the elastography inverse problem in two dimensions. *Inverse Problems*. 20: 283.
3. Calo', M.C. and Dorbath, F. and Cornet, and N. Cuenot (2011). Large-scale aseismic motion identified through 4-d p-wave tomography. *Geophys. J. Int. 186*:1295–1314.
4. Cook, N.G.W. 1992. Natural joints in rock: Mechanical, hydraulic and seismic behaviour and properties under normal stress. *Int. J. Rock Mech. Min. Sci.* 29: 198-223.
5. Eberhardt, E., D. Stead, and J.S. Coggan. 2004. Numerical analysis of initiation and progressive failure in natural rock slopes – the 1991 Randa rockslide. *Int. J. Rock Mech. Min. Sci.* 41: 69-87.
6. Gu, W.H., N.R. Morgenstern, and P.K. Robertson. 1993. Progressive failure of lower San Fernando dam. *J. Geotech. Eng.* 119: 333-349.
7. Hedayat, A., L.J. Pyrak-Nolte, and A. Bobet. 2014. Precursors to the shear failure of rock discontinuities. *Geophys. Res. Lett.* 41: 5467-5475.
8. Knight, R., L.J. Pyrak-Nolte, L. Slater, E. Atekwana, A. Endres, J. Geller, D. Lesmes, S. Nakagawa, A. Revil, M. M. Sharma, and C. Straley. 2010. Geophysics at the interface: response of geophysical properties to solid-fluid, fluid-fluid, and solid-solid interfaces. *Reviews Geophysics*. 48.
9. McLaskey, G.C., A.M. Thomas, S.D. Glaser, and R.M. Nadeau. 2012. Fault healing promotes high-frequency earthquakes in laboratory experiments and on natural faults. *Nature.* 491: 101-104.
10. Ophir, J., S.K. Alam, B. Garra, F. Kallel, E. Konofagou, T. Krouskop, T. Varghese. 1999. *Proc. Inst. Mech. Eng. H J. Eng.* 213: 203-233.
11. Place, J., O. Blake, D. Faulkner, and A. Rietbrock. 2014. Wet fault or dry fault? A laboratory approach to remotely monitor the hydro-mechanical state of a discontinuity using controlled-source seismics. *Pure Appl. Geophysics*.
12. Pourahmadian, F., and B.B. Guzina. 2015. On the elastic-wave imaging and characterization of fractures with specific stiffness. *Int. J. Solids Struct*. 71: 126-140.
13. Pourahmadian, F., and B.B. Guzina. 2016. Active ultrasonic imaging and interfacial characterization of stationary and evolving fractures in rock. *American Rock Mechanics Association Symposium*. ARMA 16-803.
14. Pourahmadian, F., H. Ahmadian, and H. Jalali. 2012. Modeling and identification of frictional forces at a contact interface experiencing micro-vibro-impacts. *J. Sound Vib.* 331: 2874-2886.
15. Pyrak-Nolte, L.J., and D.D. Nolte. 2016. Approaching a universal scaling relationship between fracture stiffness and fluid flow. *Nat. Commun.* 7: 10663.
16. Pyrak-Nolte, L.J. and J.P. Morris. 2000. Single fractures under normal stress: The relation between fracture specific stiffness and fluid flow. *Int. J. Rock Mech. Min. Sci.* 37: 245-262.

17. Schoenberg, M. 1980. Elastic wave behavior across linear slip interfaces. *J. Acoust. Soc. Am.* 68: 1516-1521.

18. Taron, J. and D. Elsworth. 2010. Coupled mechanical and chemical processes in engineered geothermal reservoirs with dynamic permeability. *Int. J. Rock Mech. Min. Sci.* 47: 1339-1348.

19. Tokmashev, R.D., A. Tixier, and B.B. Guzina. 2013. Experimental validation of the topological sensitivity approach to elastic-wave imaging. *Inverse Problems.* 29: 125005.

20. Verdon, J.P. and A.Wustefeld. 2013. Measurement of the normal/tangential fracture compliance ratio (z_N/z_T) during hydraulic fracture stimulation using S-wave splitting data. *Geophys. Prospecting.* 61: 461-475.

21. Zietlow, W.K. and Labuz, J.F. (1998). Measurement of the intrinsic process zone in rock using acoustic emission. *Int. J. Rock Mech. Min. Sci.* 35: 291-299.